Int. J. Electrochem. Sci., 10 **(2015)** 2000 - 2013

International Journal of
ELECTROCHEMICAL
SCIENCE
www.electrochemsci.org

Manganese Oxide Nanorods Supported on Orange Peel-Based Carbon Nanosheets for High Performance Supercapacitors

Kanjun Sun[1,2,*], *Haiping Wang*[2], *Hui Peng*[2], *Yajuan Wu*[2], *Guofu Ma*[2], *Ziqiang Lei*[2,]

[1] College of Chemistry and Environmental Science, Lanzhou City University, Lanzhou 730070, China.
[2] Key Laboratory of Eco-Environment-Related Polymer Materials of Ministry of Education, Key Laboratory of Polymer Materials of Gansu Province, College of Chemistry and Chemical Engineering, Northwest Normal University, Lanzhou 730070, China.
[*]E-mail: sunkj@lzcu.edu.cn

Received: 26 November 2014 / *Accepted:* 31 December 2014 / *Published:* 19 January 2015

A composite materials carbon nanosheets supported MnO_2 nanorods exhibiting high capacitance performance can be fabricated by a simple and scalable method. The carbon nanosheets are easily obtained from the orange peel by carbonization at 800 ^oC, and MnO_2 nanorods can be grown on the carbon nanosheets through the reaction between $KMnO_4$ aqueous solution and the carbon. The electrochemical studies showed that the supercapacitor based on the hybrid materials with MnO_2 content of 3.8 % exhibited the largest specific capacitance of 656 F g^{-1} at a current density of 1 A g^{-1}, after 5000 cycles, the capacitance still retention above 80%. In addition, after MnO_2 nanorods attached onto the carbon nanosheets layer, the BET specific surface area of this hybrid materials is improved to 573 m^2 g^{-1}, the addition of carbon nanosheets as a conducting agent improves the high-rate capability considerably, and the MnO_2 nanorods crystals in turn is of great benefit to further exfoliating carbon nanosheets, which give the composite potential application as high-performance supercapacitor electrode materials.

Keywords: Manganese Oxide nanorods. Carbon nanosheets. Electrode materials. Conductivity. Supercapacitor.

1. INTRODUCTION

The present day technological society demands energy storage devices for various portable electronic devices and hybrid motor vehicles. In this regard, different kinds of batteries and high-performance capacitors are the focus of current scientific research [1, 2]. Electrochemical capacitors (ECs or so-called supercapacitors) are promising energy storage devices, which have garnered interest due to their high power density, quick charging, long cycling life, and great reversibility [3, 4]. Since

the electrode materials are the most important factor in determining the properties of supercapacitors. In contrast to conventional carbon-based materials, metal oxides electrode materials have much larger specific capacitance owing to their significant redox pseudocapacitance properties. Among the transition metal oxides, manganese dioxide (MnO_2) is one of the most promising pseudocapacitive materials show many significant advantages such as wide potential range, low cost, abundance in nature and environmental friendliness [5]. In fact, the theoretical specific capacitances of MnO_2 reach up to 1370 F g^{-1} based on a one-electron redox reaction per manganese atom. However, hydrated MnO_2 with various structures often exhibit low specific capacitances general less than 200 F g^{-1} [6, 7]. The limited extracted capacitance is likely due to MnO_2 low-electron and limited ion conductances [8]. To improve the electrical conductivity of the MnO_2, several strategies have been proposed, for instance, incorporating MnO_2 with carbon-based materials such as graphene, graphene oxide, carbon nanotubes (CNTs), carbon aerogels and activated carbons [9-12]. However, activated carbon has its potential in many applications and devices, especially, the activated carbons have been obtained by pyrolysis of biomass precursors [13, 14] due to they are comparatively cheap and porous, which resulting in good electrochemical capacitive performance.

Orange, specifically known as citrus sinensis, is one of the most favored subtropical fruits in the world, and it is also available in the processing industries [15]. It has been found that orange peel principally consists of cellulose, pectin, hemi-cellulose, lignin, chlorophyll pigmentsand and other low molecular weight hydro-carbons. These components contain various functional groups, which have interested several fields such as agro-industry [16, 17], cosmetics [18], flavoring [19] and pharmaceutical [20]. Utilization of orange peel as precursor for activated carbon with a high surface area has already been demonstrated [21].

In this paper, the orange peel was utilized as raw materials to preparation the carbon nanosheets, which used as substrate to grow MnO_2 nanorods. Through redox reaction and adjusting the ratio of $KMnO_4$ to the carbon, the carbon materials supported by MnO_2 nanorods composite with different MnO_2 content was prepared. Electrochemical tests indicate that weight ratio of carbon to $KMnO_4$ at 4:1 had high specific surface area and excellent supercapacitor performance. In addition, this method presents a promising general route for the large-scale production of the carbon nanosheet supported MnO_2 nanorods composite as energy storage materials.

2. EXPERIMENTAL

2.1. Preparation Orange peel-based activated carbons (OAC)

Orange peel was obtained from a local fruit field. The peel was washed to remove the adhering dirt and then dried at room temperature 60 ^oC for 36 h. The dried orange peel was carbonized between 600 and 900 ^oC with temperature ramp rate of 5 ^oC min^{-1} and kept for 2.5 h under nitrogen atmosphere in a tubular furnace. The carbonization product was washed in 0.5 M HCl solution and distilled water several times, then filtered and dried at 60 ^oC . The resultant samples at different carbonization temperature from 600 to 900 ^oC were labeled as OAC-6, OAC-7, OAC-8 and OAC-9, respectively.

2.2. Fabrication of MnO_2/OAC-8 composite

The MnO_2/OAC-8 composite was prepared as follows: 0.2 g of the as-prepared OAC-8 was first immersed in 100 mL $KMnO_4$ aqueous solution in a glass flask. Then, the obtained dispersive solution was heated to 80 ^oC in an oil bath for 12 h. Finally, the products were collected by decanting the upper solution, rinsed with water and dried at 60 ^oC. A series of MnO_2/OAC-8 composites were prepared by controlling the weight ratio of OAC-8 to $KMnO_4$ at 4:1, 2:1, 1:1 and 1:2. The composites were denoted as OM1, OM2, OM3 and OM4, respectively.

2.3 Characterization

X-ray diffraction (XRD) of samples was performed on a diffractometer (D/Max-2400, Rigaku) advance instrument using Cu Kα radiation (k=1.5418 Å) at 40 kV, 100 mA. The 2θ range used in the measurements was from 5 to 80°. Raman spectra of samples were taken on a RFS-100 (Bruker) with an excitation length of 1024.5 nm. Thermogravimetric analyses (TGA) of samples was performed on a STA449-C thermogravimetric analyzer from 25 to 900 °C at a heating rate of 10 °C min^{-1} in air flow. N_2 adsorption-desorption isotherms were measured using a Micromeritics ASAP 2020 Analyzer (U.S.A.). Pore sizes were calculated by the Barrett, Joyner, and Halenda (BJH) method. The structure and morphology of the samples were examined with field emission scanning electron microscopy (FESEM, JSM-6701F, Japan) at an accelerating voltage of 5.0 kV and transmission electron microscopy (TEM, JEM-2010 Japan). Selected area electron diffraction (SAED) patterns were also obtained on JEM-2010 transmission electron microscope with the acceleration voltage of 200 kV.

2.4. Electrochemical measurements

The electrochemical measurements were performed using a CHI 660D electrochemical work station interfaced to a computer system with corresponding electrochemical software. Electrodes were prepared by mixing 90 wt.% achieved samples, 5 wt.% carbon black (Mitsubishi #32) and 5 wt.% polytetrafluoroethylene (PTFE) to form slurry, then the obtained slurry was coated on a nickel foam substrate with an area of 1 cm^2, dried, and pressed under a pressure of 20 MPa to form a thin sheet (thicnkess of about 0.2 mm). In a typical three electrode system, the above loaded nickel foam as working electrode was investigated with a Pt counter electrode and Hg/HgO reference electrode in 6 M KOH solution electrolyte.

3. RESULTS AND DISCUSSION

3.1. Morphological Analysis

A powder X-ray diffraction (XRD) experiment was carried out to gain insight into the internal structure of the OAC, and MnO_2/OAC-8 composites. Fig. 1a exhibit OAC diffraction pattern centered

at around 23° and 43°, which are assigned to the (002) and (100) diffractions of the graphitic framework [22-24], as can be seen the (002) peak of OAC-8 much sharper than the others, indicating an increase in the degree of graphitization.

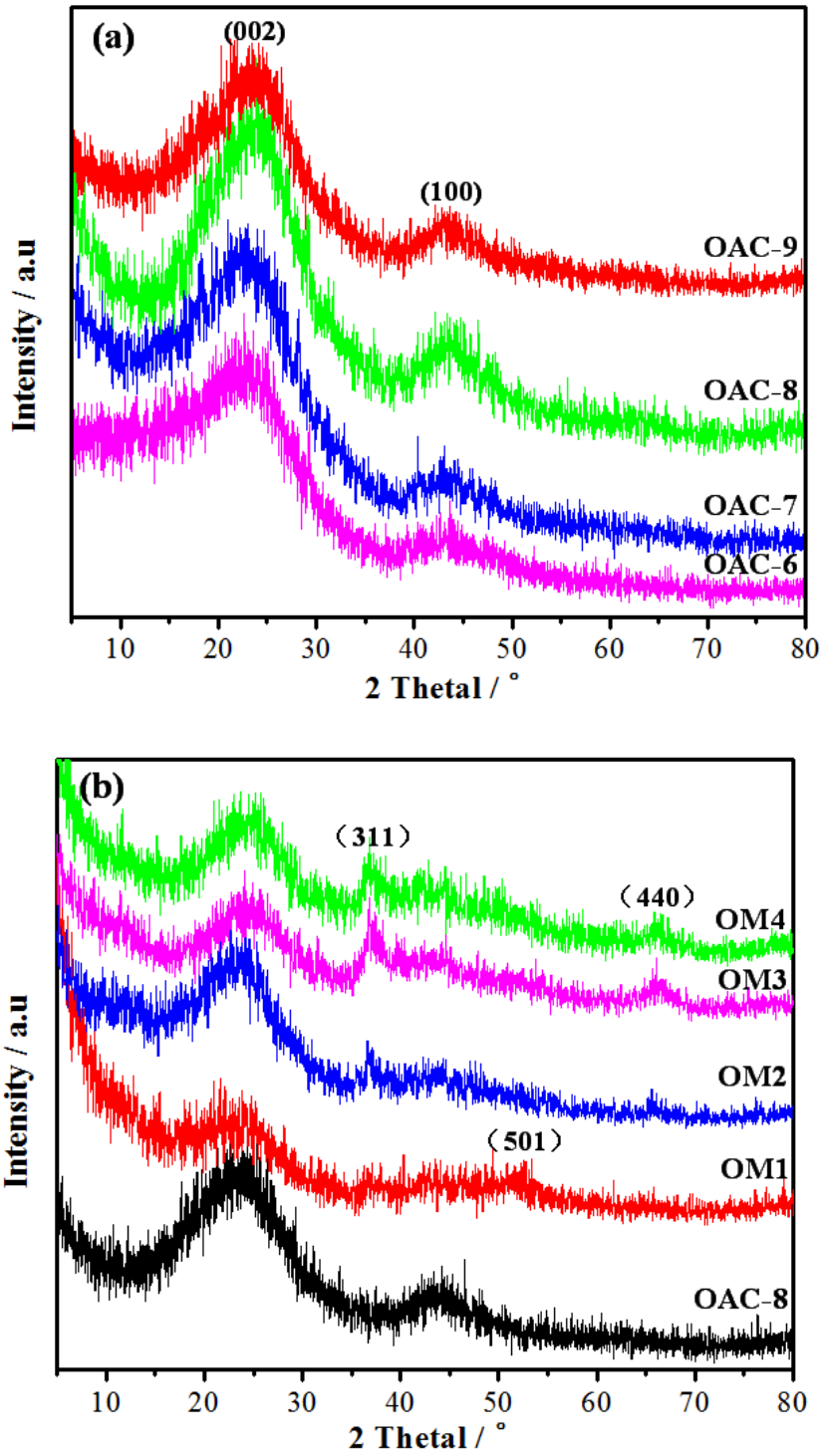

Figure 1. (a) XRD patterns of the OAC prepared at different carbonization temperature; (b) XRD patterns of OAC-8, OM1, OM2, OM3 and OM4.

In Fig. 1b, comparison of XRD spectrum for OM1, OM2, OM3, OM4 and OAC-8, and the solids are XRD amorphous or very poorly crystalline, it shows a typical broad and weak reflection located in the range of 15-30°, which are the characteristic peak of amorphous graphitic. The main diffraction peaks at 2θ values for 37° and 65° demonstrate crystalline planes (311) and (440) of MnO_2 (JCPDS 42-1169). Broad peaks are related to a poorly crystallized compound, compared to samples OM2, OM3, OM4 the samples of OM1 peaks at 2θ=53° exposed small (501) facets of MnO_2 ramsdellite (JCPDS 39-0375). Morphologically, MnO_2 crystals consist of [MnO_6] octahedra with shared vertices and edges. Stacking of [MnO_6] octahedra enables the building of one-dimensional MnO_2 ramsdellite (γ-MnO_2). MnO_2 electrodes with larger tunnel sizes favored the storage of alkaline cations (e.g., Na^+, K^+, Li^+) and exhibited higher capacitance [25-27].

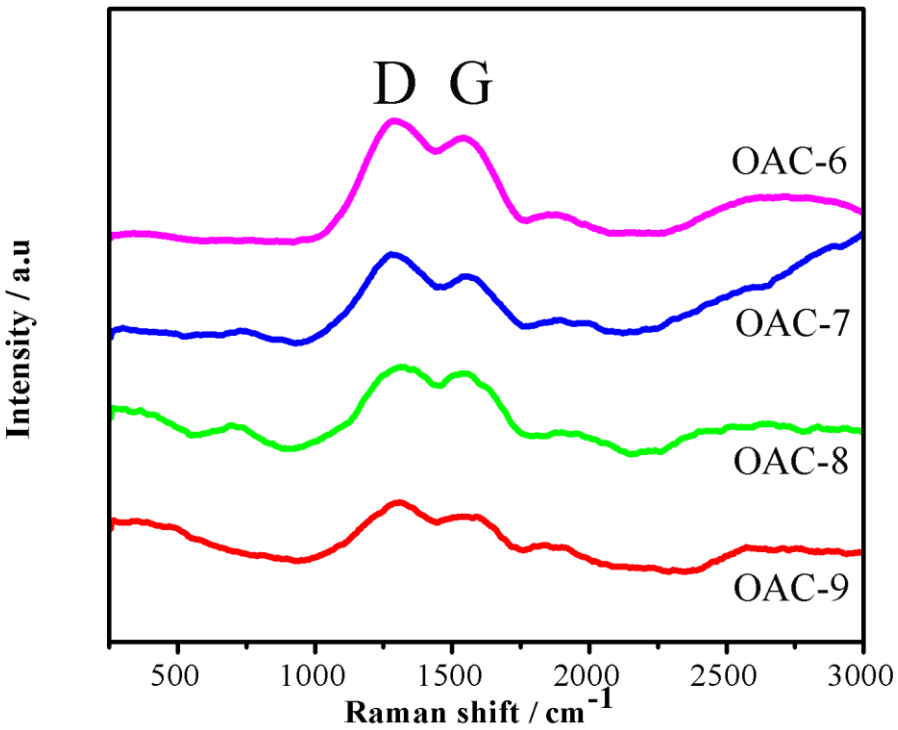

Figure 2. Raman spectra of OAC prepared at different carbonization temperature.

Fig. 2 shows the Raman spectra of OAC prepared at different carbonization temperatures. Two peaks at ~1300 cm^{-1} and ~1600 cm^{-1} could be observed in the Raman spectra of all the OAC. The former corresponds to D band showing the presence of defects in the graphitic lattice with A_{1g} symmetry, while the latter peak, namely, G band, is associated with the in-plane E_{2g} mode of single crystalline graphitic carbon atoms in the honeycomb lattice [28, 29]. The intensity ratio of D-band to G-band (I_D/I_G) depends on the type of graphitic materials and reflects the graphitization degree. The values of I_D/I_G for OAC-6, OAC-7, OAC-8, and OAC-9 are 1.197, 1.431, 1.081, and 1.123, and the relatively lower I_D/I_G value of OAC-8 indicating the higher degree of graphitization, which is well consistent with the XRD observations.

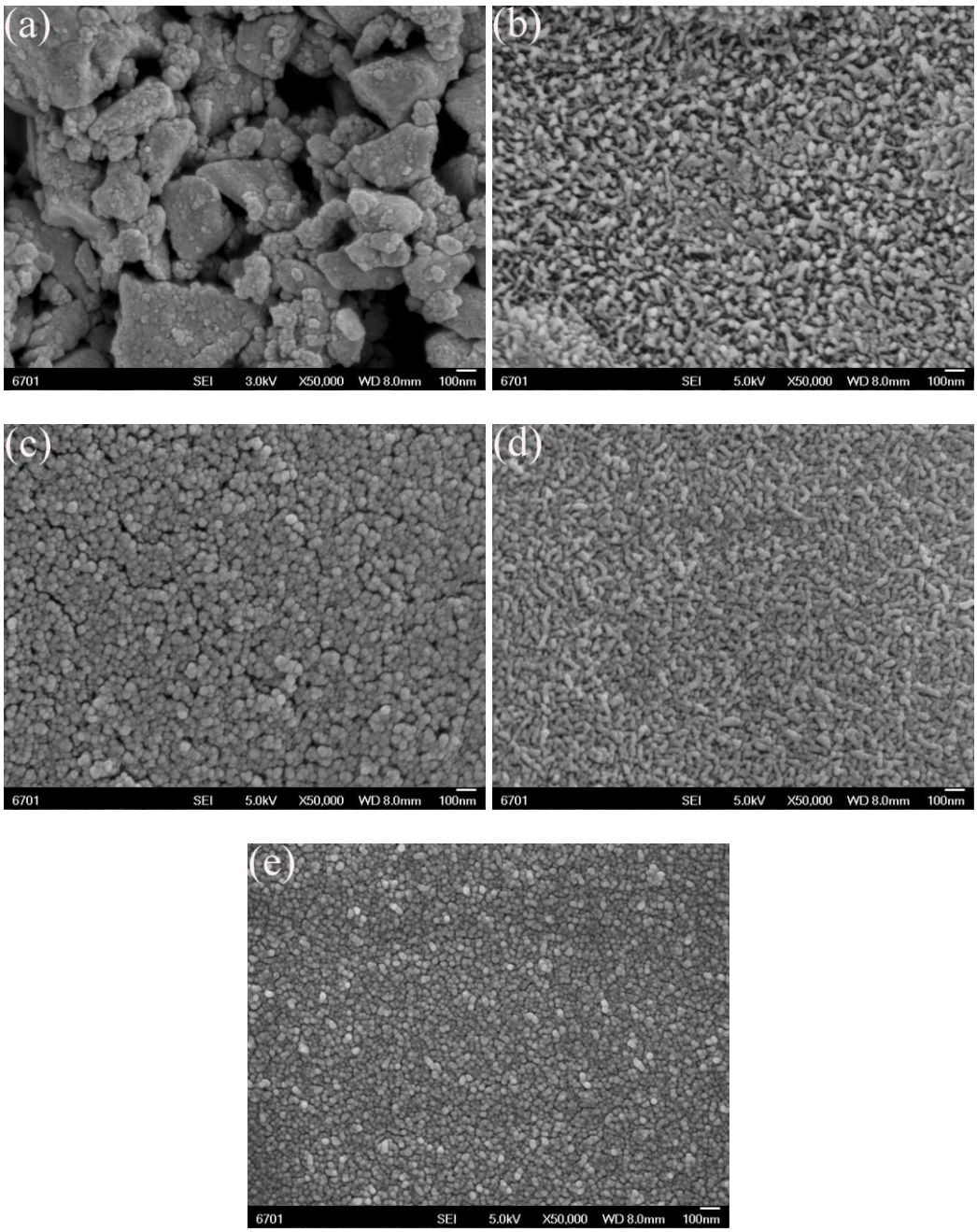

Figure 3. SEM images of (a) OAC-8, (b) OM1, (c) OM2, (d) OM3 and (e) OM4.

Fig. 3a shows the FE-SEM image of OAC-8, it is very obvious that the image display a disordered crude solid particles microstructure. Fig.3b, c, d and e show the images of the OM1, OM2, OM3 and OM4, respectively. It can be seen that after the growing of MnO_2 on the nanosheets of the OAC-8, the OM1 composite formed interconnected rod-like architectures structures, though the rod surface is not very smooth, no obvious pores exists, but, by means of irregular pile-up, these rod-like architectures structures constructed a complex three-dimensional porous microstructure. However, for the OM2, OM3 and OM4 samples, with the amount of $KMnO_4$ increased, the rod-like structures become smaller, and a large quantity of nanospheres can be found. This change can be ascribed to the

relatively high concentration of $KMnO_4$ which leads to the rapid reaction between $KMnO_4$ and OAC-8, and the quick formation of MnO_2 nucleus on the nanosheets of the OAC-8 by the following redox reaction [30]:

$$4MnO_4^- + 3C + H_2O = 4MnO_2 + CO_3^{2-} + 2HCO_3^- \quad (1)$$

Thermogravimetric analysis (TGA) was performed to analyze the composition of the composites. The weight percents of MnO_2 in OM1, OM2, OM3, OM4 samples were obtained as 3.8%, 7.5%, 13.7% and 21.0% (Fig. 4).

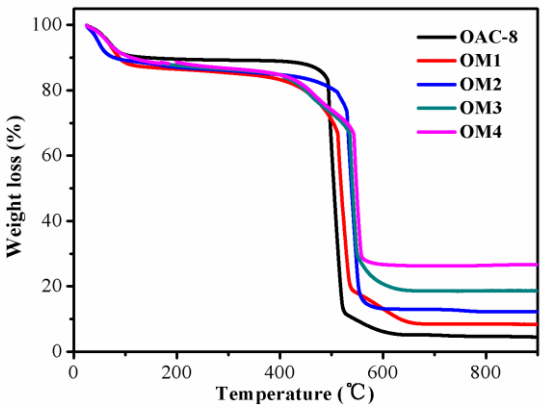

Figure 4. TGA curves of OAC-8, OM1, OM2, OM3, OM4.

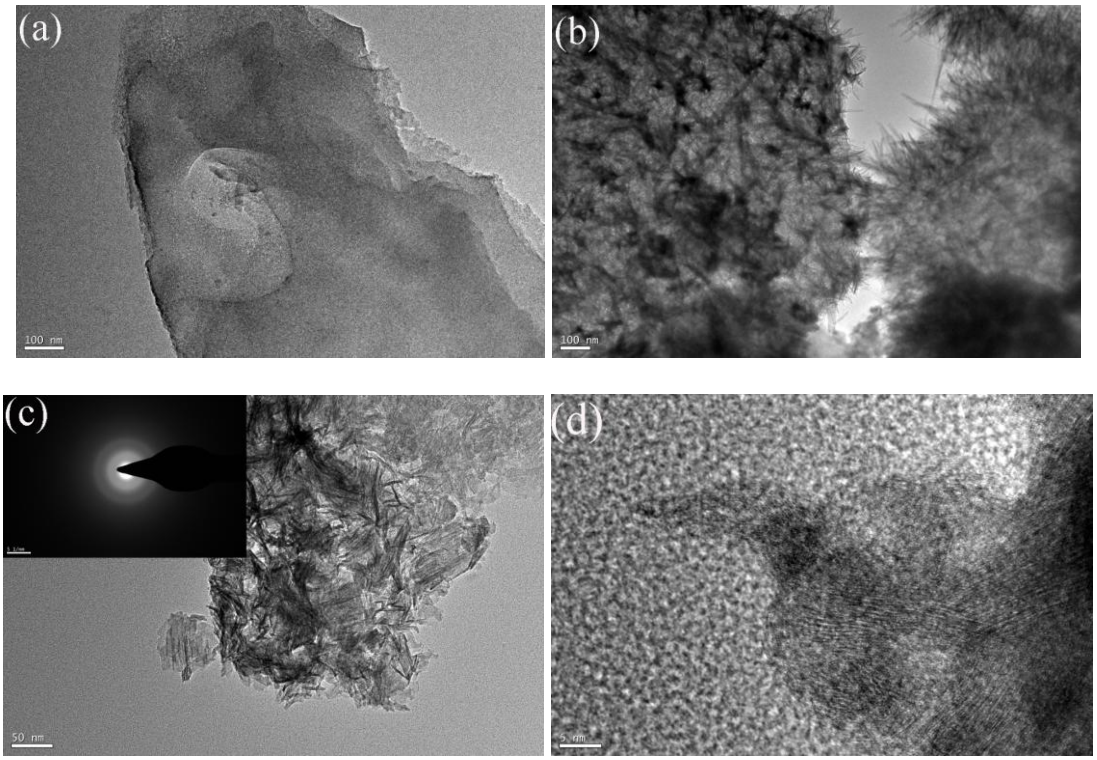

Figure 5. (a) TEM image of OAC-8; (b, c) Low- and (d) high-resolution TEM images of OM1, inset in (c) shows the SAED of OM1.

Such result indicates that MnO_2 content in the composites increases with the increasing of $KMnO_4$ concentration. The TEM images clearly demonstrate the structure and morphology of the OAC-8 and OM1 (Fig. 5a, b, c and d). From Fig. 5a, we can find the OAC-8 exhibited two-dimensional plate-like nanosheets structure. After reaction with $KMnO_4$, the rod-like architectures structures was formed on the nanosheets of the OAC-8 (Fig. 5b). The small crystal size does not allow the selected area electron diffractio (SAED) examination focused on single MnO_2 nanoparticles. Therefore, the SAED pattern displays a polycrystalline feature due to the random orientation of different MnO_2 nanoparticles (Fig. 5c, inset). Moreover, low- and high-resolution TEM shows that the crystallinity of MnO_2 ramsdellite nanorods on the carbon nanosheets surface is not very high (Fig. 5c and d), this is consistent with the XRD results. It is believed that, on the one hand, the assembly of nanorods structures to some extent prevents the stacking of carbon nanosheets due to van der Waals interactions, leading to a large available surface area and rich porous structure for energy storage, while on the other hand, the presence of carbon nanosheets with high electrical conductivity is favorable to improve the dispersion of MnO_2 nanorods and the electrical conductivity of the composite electrode [31].

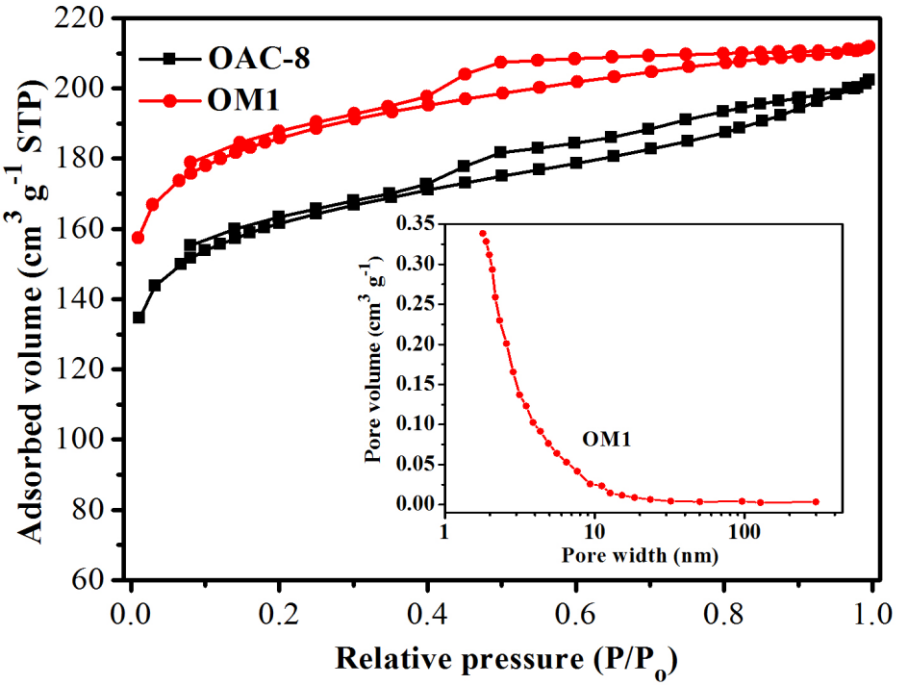

Figure 6. Nitrogen adsorption-desorption isotherms of OAC-8 and OM1. The inset shows the pore size distribution curve of OM1.

The BET measurements were performed to investigate the textural characteristics of OAC-8 and OM1. The N_2 adsorption-desorption isotherms are shown in Fig. 6, where the inset shows the pore size distribution of OM1 composite obtained from the analysis of N_2 desorption isotherms by using the

BJH method. The BET specific surface area, pore volume and average pore size of the OAC-8 and OM1 composite are summarized in Table 1.

Table 1. The BET specific surface areas, average pore size, and pore volumes of OAC-8 and OM1.

Samples	S_{BET} (m^2 g^{-1})	Average pore size (nm)	Pore volume (cm^3 g^{-1})
OAC-8	500	2.5	0.31
OM1	573	2.3	0.33

The measured BET specific surface area of OAC-8 is 500 m^2 g^{-1}, after MnO_2 nanorods attached onto the OAC-8 nanosheets, the BET specific surface area of OM1 is improved to 573 m^2 g^{-1}. However, as shown in the pore size distribution of the OM1 composite, which indicates the presence of mainly numerous micropores (below 2 nm) and mesopores, and the possibility of macropores (inset of Fig. 6). These results demonstrate the existence of some porous structures in the OM1 composite. Furthermore, this specific structure will provide the possibility of efficient electron transfer and electrolyte diffusion.

3.2. Electrochemical properties

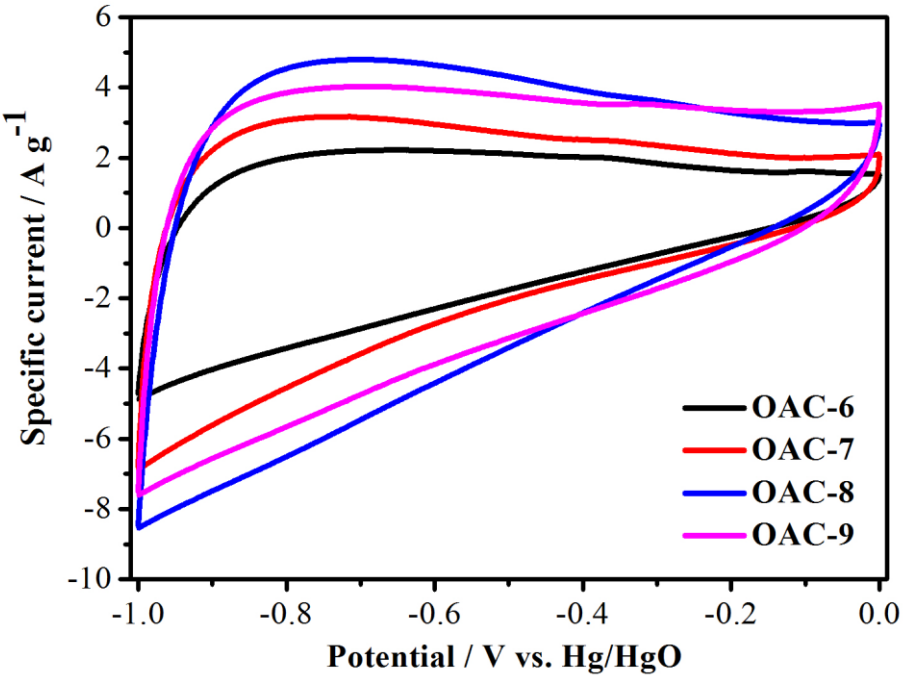

Figure 7. CV curves of OAC-6, OAC-7, OAC-8, and OAC-9 within the potential window -1.0-0 V at a scan rate of 50 mV s^{-1} in 6 M KOH electrolyte.

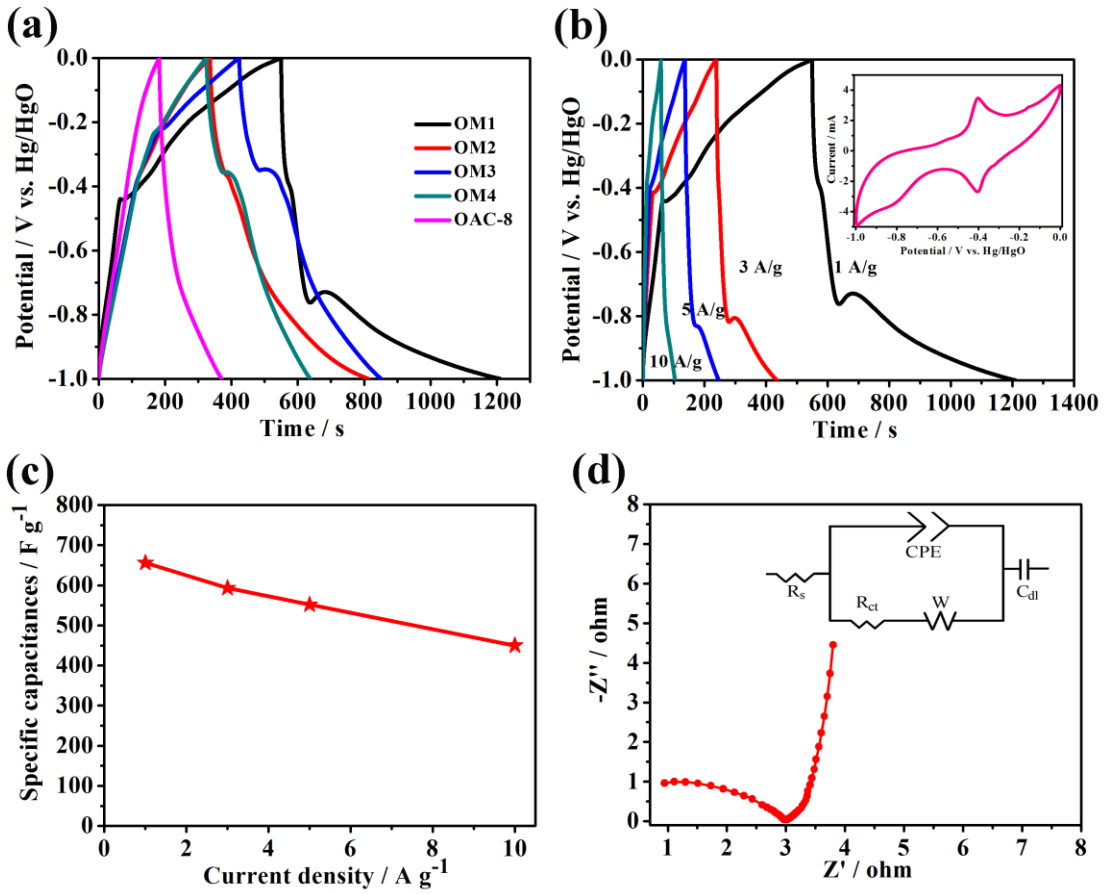

Figure 8. (a) Galvanostatic charge-discharge curves of OAC-8, OM1, OM2, OM3 and OM4 at a current density of 1 A g^{-1}; (b) charge-discharge curves of OM1 at a current density of 1-10 A g^{-1}. Inset shows the CV profile for the OM1 recorded at a scan rate of 10 mV s^{-1}; (c) the corresponding discharge capacitances; (d) Nyquist plots of OM1. The inset is the equivalent circuit.

To evaluate the potential applications of the OAC, the cyclic voltammetry (CV) curves of the OAC-6, OAC-7, OAC-8 and OAC-9 are presented in Fig. 7 at a scanning rate 50 mV s^{-1} in a potential window of -1.0 to 0 V. As can be seen, all samples show nearly rectangular CV curve without any redox peaks, which indicates the OAC only electrical double-layer capacitance. Among all the samples, OAC-8 shows the highest peak current density and the largest CV area, indicating the largest electrochemical capacitance [32, 33]. Fig. 8a gives the galvanostatic charge-discharge curves of OAC-8, OM1, OM2, OM3 and OM4 at a current density of 1 A g^{-1}. The specific capacitance of the electrode can be calculated using the following equation [34]:

$$C_m = C / m = (I\,t) / (\Delta V\,m) \quad (2)$$

Where C_m is specific capacitance (F g^{-1}), I is charge-discharge current (A), t is the time of discharge (s), ΔV is the voltage difference between the upper and lower potential limits, and m is the mass of the active electrode material. The specific capacitance of all the sample at the current density of 1 A g^{-1} was calculated according to Eq.(2) , the corresponding gravimetric capacitances are 188 F g^{-1} (OAC-8), 656 F g^{-1} (OM1), 462 F g^{-1} (OM2), 435 F g^{-1} (OM3) and 316 F g^{-1} (OM4). This

demonstrates the strong synergistic effect of the combined capacitive contributions from the MnO_2 and OAC-8. In order to further evaluate the electrochemical capacitance of the optimized OM1, the galvanostatic charge-discharge curves were measured at various current densities of 1, 3, 5, and 10 A g^{-1} (Fig. 8b). The CV profile for the OM1 electrode recorded at a scan rate of 10 mV s^{-1} (inset of Fig. 8b). The voltammetric profile is very similar to those found in the literatures [35-37] and the voltammetric peaks are associated to a series of redox processes [38,40]. These processes are composed of several steps and the corresponding voltammetric peaks are overlapped and difficult to identify or to associate with a specific process. Meanwhile the main reactions are those associated to the two consecutive steps involving Mn^{IV}/Mn^{III} and Mn^{III}/Mn^{II} [41,42]. The discharge capacitances at various current densities are plotted in Fig. 8c. It is evident that the capacitance of this composite slowly decreases as the current density increases from 1 to 10 A g^{-1}, and the specific capacitance of the OM1 composite still retains ~70% of the original value. The high performance of OM1 is mainly attributed to the ramsdellite particular properties of MnO_2 and even the synergistic effects of the MnO_2 and OAC-8. The interconnected MnO_2 nanorods provides a special high surface area and rich pore structures, which are very important for ensuring more electroactive sites for the adsorption of K^+ and hence enhancing the utilization of active materials during the charge-discharge process [43, 44]. The OAC-8 here has dual functions, which can not only contribute high specific capacitance to the composite, but can also serve as a conductive path for electron transport due to its high conductivity.

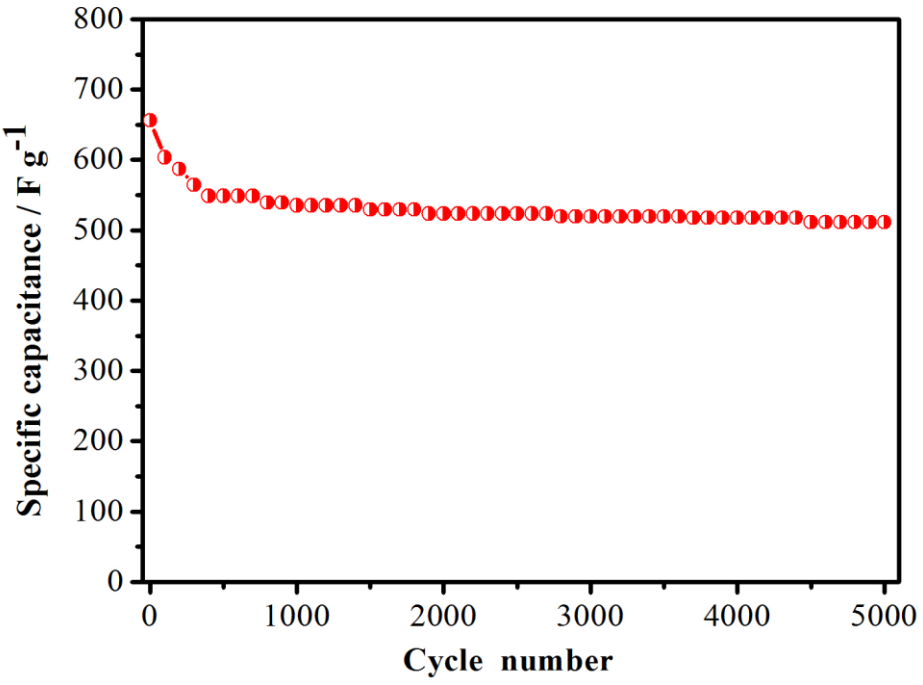

Figure 9. Cycling stability of OM1 at a current density of 1 A g^{-1} in the long-term cycle.

Fig. 8d represents the complex-plane electrochemical impedance spectrum (EIS) of the OM1 nanocomposite electrode based supercapacitor. Electrochemical impedance spectra measurements were carried out at the open-circuit potential over a frequency range of 100 kHz to 100 mHz, with the

electrical circuit in the inset. The equivalent electrical circuit consists of a resistive element (R_s) in a series combination with (CPE/(R_{ct} +W_d)) and a double-layer capacitor (C_{dl}). The impedance spectrum has a semicircular arc and a straight line. At very high frequencies, the intercept at real part (Z') represents a combined resistance of ionic resistance of electrolyte, intrinsic resistance of substrate, and contact resistance at the active material/current collector interface (R_s) was calculated to be 0.54 ohm, indicating a low internal resistance for the whole device. The charge transfer resistance (R_{ct}) caused by the Faradaic reactions and the double-layer capacitance (C_{dl}) at the contact interface between electrode and electrolyte solution. R_{ct} can be directly measured as the semicircular arc diameter. The 45° slope portion of the curve is the Wurburg resistance (Z_w), which is a result of the frequency dependence of ionic diffusion/transport in the electrolyte and to the surface of the electrode [45-47]. Moreover, at low frequencies, the straight line of OM1 is nearly perpendicular to the realy axis, demonstrating it had pure capacitive behaviors [48].

A long cycle life is another crucial parameter of supercapacitors, which can determine their practical applications. Hence, the stability of the supercapacitors based on the OM1 composite was tested in the range of -1.0 and 0 V at 1 A g^{-1} in 6 M KOH aqueous solution (Fig. 9). The results indicate the OM1 composite has good cycling ability, the capacitive retention of the OM1 composite is 512 F g^{-1} about 80% of the initial capacitance after 5000 cycles. This result indicates that the OM1 composite can be considered as promising electrode in the application of high performance energy-storage devices.

4. CONCLUSIONS

In summary, the prepared orange peel-based carbon nanosheets supported MnO_2 nanorods composite have been successfully employed as supercapacitor electrodes and give a highest specific capacitance (656 F g^{-1}) and cycling stability (the capacitance still retention above 80% after 5000 cycles). The high specific capacitance and good cycle ability coupled with the low cost and environmentally benign nature of the carbon supported MnO_2 composite may make this material attractive for large applications.

ACKNOWLEDGEMENTS
We thank the Science and Technology program of Gansu Province (NO.1308RJZA295, 1308RJZA265), the program for Changjiang Scholars and Innovative Research Team in University (IRT1177), the Colleges and Universities Scientific Research program of Gansu Province (2013B-069), PhD Scientific Research starting Program of Lanzhou City University (LZCU-BS2013-11), Key Laboratory of Eco-Environment-Related Polymer Materials of Ministry of Education, and Key Laboratory of Polymer Materials of Gansu Province.

References

1. J. R. Miller and P. Simon, *Science*, 321 **(**2008) 651.

2. S.M. Chen, R. Ramachandran, V. Mani, R. Saraswathi, *International Journal of Electrochemical Science*, 9 (2014) 4072.
3. A. L. M. Reddy, S. R. Gowda, M. M. Shaijumon and P. M. Ajayan, *Advanced Materials*, 24 (2012) 5045.
4. V. Srinivasan and J. W. Weidner, *Journal of the Electrochemical Society*, 146 (1999) 1650.
5. Y. He, W. Chen, X. Li, Z. Zhang, J. Fu, C. Zhao and E. Xie, *ACS Nano*, **7** (2012) 174.
6. H. Gao, F. Xiao, C. B. Ching and H. W. Duan, *ACS Applied Materis & Interfaces*, 4 (2012) 2801.
7. G. R. Li, Z. P. Feng, Y. N. Ou, D. C. Wu, R. W. Fu and Y. X. Tong, *Langmuir*, 26 (2010) 2209.
8. J. N. Broughton and M. J. Brett, *Electrochimica Acta*, 50 (2005) 4814.
9. Y. Wang, S. F. Yu, C. Y. Sun, T. J. Zhu and H. Y. Yang, *Journal of Materials Chemistry*, 22 (2012) 17584.
10. L. Chen, Y. Hernandez, X. Feng and K. Müllen, *Angewandte Chemie-International Edition*, 51 (2012) 7640.
11. L. Wei and G. Yushin, *Nano Energy*, 1 (2012) 552.
12. M. Yang, J. X. Li, H. H. Li, L. W. Su, J. P. Wei and Z. Zhou, *Physical Chemistry Chemical Physics*, 14 (2012) 11048.
13. S. M. Heilmann, H. T. Davis, L. R. Jader, P. A. Lefebvre, M. J. Sadowskyd, F. J. Schendel, M. J. Von Keitza and K. J. Valentas, *Biomass and Bioenergy*, 34 (2010) 875.
14. E. Raymundo-Piñero, M. Cadek and F. Béguin, *Advanced Functional Materials*, 19 (2009) 1032.
15. R. J. Braddock, *Food Technology*, 49 (1995) 74.
16. K. Y. Foo and B. H. Hameed, *Bioresource Technology*, 104 (2012) 679.
17. M. R. Mafra, L. Igarashi-Mafra, D. R. Zuim, É. C. Vasques and M. A. Ferreira, *Brazilian Journal of Chemical Engineering*, 30 (2013) 657.
18. T. Allaf, V. Tomao, C. Besombes and F. Chematet, *Chemical Engineering and Processing*, 72 (2013) 24.
19. S. Sawalha, D. Arráez-Román, A. Segura-Carretero and A. Fernández-Gutiérrez, *Food Chemistry*, 116 (2009) 567.
20. B. Liu, G. Han, Z. Zhang, R. Liu, C. Jiang, S. Wang and M. Y. Han, *Analytical Chemistry*, 84 (2011) 255.
21. A. A. Arie, H. Kristianto and J. K. Lee, *ECS Transactions*, 53 (2013) 9.
22. D. Hulicova-Jurcakova, M. Seredych, Y. Jin, G.Q. Lu and T.J. Bandosz, *Carbon*, 48 (2010) 1767.
23. M. Inagaki, H Konno and O. Tanaike, *Journal of Power Sources*, 195 (2010) 7880.
24. S. H. Mujawar, S. B. Ambade, T. Battumur, R. B. Ambade and S. H. Lee, *Electrochimica Acta*, 56 (2011) 4462.
25. A. L. M. Reddy and S. Ramaprabhu, *Journal of Physical Chemistry C*, 111 (2007), 7727.
26. S. Devaraj and N. Munichandraiah, *Journal of Physical Chemistry C*. 112 (2008) 4406.
27. S. Chen, J. Zhu, X. Wu, Q. Han and X. Wang, *ACS Nano*, 4 (2010) 2822.
28. D. Y. Qu, *Journal of Power Sources*, 109 (2002) 403.
29. I. Calizo, A. A. Balandin, W. Bao, F. Miao and C. N. Lau, *Nano Letters*, 7 (2007) 2645.
30. X. Huang, H. Yue, A. Attia and Y. Yang, *Journal of the Electrochemical Society*, 154 (2007) A26.
31. K. Chen, Y. Dong, K. Li, S. Komarneni and D. Xue, *Journal of Physical Chemistry C*, 117 (2013) 10770.
32. E. Raymundo-Piñero, F. Leroux and F. Béguin, *Advanced Materials*, 18 (2006) 1877.
33. D. D. Zhao, S. J. Bao, W. J. Zhou and H. L. Li, *Electrochemistry Communications*, 9 (2007) 869.
34. H. Jiang, C. Li, T. Sun and J. Ma, *Chemical Communications*, 48 (2012) 2606.
35. J. McBreen, *Electrochimica Acta*, 20 (1975) 221.
36. P. Bezdicka, T. Grygar, B. Klapste and J. Vondr´ak, *Electrochimica Acta*, 45 (1999) 913.
37. P. Ruetschi, *Journal of the Electrochemical Society*, 131 (1984) 2737.
38. Y. Chabre and J. Pannetier, *Progress in Solid State Chemistry*, 23 (1995) 1.

39. L. Mao, D. Zhang, T. Sotomura, K. Nakatsu, N. Koshiba and T. Ohsaka, *Electrochimica Acta*, 48 (2003) 1015.
40. F. H. B. Lima, M. L. Calegaro and E. A. Ticianelli, *Electrochimica Acta*, 52 **(**2007) 3732.
41. P. Bezdička, T. Grygar, B. Klápště and J. Vondrák, *Electrochimica Acta*, 45 (1999) 913.
42. M. L. Calegaro, F. H. B. Lima and E. A. Ticianelli, *Journal of Power Sources*, 158 (2006) 735.
43. O. Ghodbane, J. L. Pascal and F. Favier, *ACS Applied Materis & Interfaces*, 1 (2009) 1130.
44. S. Chen, J. Zhu, Q. Han, Z. Zheng, Y. Yang and X. Wang, *Crystal Growth & Design*, 9 (2009) 4356.
45. M. D. Stoller, S. J. Park, Y. W. Zhu, J. H. An and R. S. Ruoff, *Nano Letters*, 8 (2008) 3498.
46. A. Di Fabio, A. Giorgi, M. Mastragostino and F. Soavi, *Journal of the Electrochemical Society*, 148 (2001) A845.
47. P. Yang, X. Xiao, Y. Li, Y. Ding, P. Qiang, X. Tan, W. Mai, Z. Lin, W. Wu, T. Li, H. Jin, P. Liu, J. Zhou, C.P. Wong and Z. L Wang, *ACS Nano*, **7** (2013) 2617.
48. J. Chen, K. Sheng, P. Luo, C. Li and G. Shi, *Advanced Materials*, 24 (2012) 4569.